AIAA JOURNAL
Vol. 43, No. 6, June 2005

Validation Study of a Multidomain Spectral Code for Simulation of Turbulent Flows

G. B. Jacobs*
Brown University, Providence, Rhode Island 02912
D. A. Kopriva†
Florida State University, Tallahassee, Florida 32306
and
F. Mashayek‡
University of Illinois at Chicago, Chicago, Illinois 60607

A Chebyshev multidomain staggered-grid method (CMSM) presented by Kopriva (Kopriva, D. A., "A Staggered-Grid Multidomain Spectral Method for the Compressible Navier–Stokes Equations," ***Journal of Computational Physics*****, Vol. 143, No. 1, 1998, pp. 125–158) for numerical simulation of three-dimensional compressible turbulent flows, is validated. Computations with the CMSM of an isotropic turbulence and a fully developed turbulent channel flow are compared with previously published results. Turbulence initiation of the isotropic turbulence on the Chebyshev grid is discussed. Low-resolution simulations ensure transition of an initial laminar channel flow to a turbulent channel flow. The turbulent kinetic energy spectrum has sufficient dropoff (indicating a resolved solution) at a minimum of 3 to 6 points per wave number for a polynomial approximation of 13 to 10, respectively.**

Nomenclature

C_p = specific heat
$E(k)$ = energy spectrum
e = energy flux
$\boldsymbol{F}, \boldsymbol{G}, \boldsymbol{H}$ = flux vector in x, y, and z directions
h_j = Lagrangian polynomial on Gauss grid
$\boldsymbol{i}$ = the imaginary number $\sqrt{-1}$
J = Jacobian
k = wave number
L = nondimensional length
L_f = reference length
l_j = Lagrangian polynomial on Lobatto grid
Ma = $uM_f/\sqrt{T}$ Mach number
M_f = $U_f/\sqrt{(\gamma R T_f)}$ reference Mach number
N = number of grid points per subdomain in each direction
$\boldsymbol{P}_N$ = space of polynomials of degree less than or equal to N
Pr = $C_p\mu/\kappa$ Prandtl number
p = $\rho T/\gamma M_f^2$ pressure
$\wp$ = approximation order
$\boldsymbol{Q}$ = vector of solution unknowns
R = gas constant
Re_f = $\rho_f U_f L_f/\mu$ reference Reynolds number
T = temperature
t = time
U_f = reference velocity
u, v, w = velocity in x, y, and z directions
u_τ = skin-friction velocity
X, Y, Z = spatial coordinates in mapped space
x, y, z = spatial coordinates in physical space
γ = ratio of the specific heats
ϵ = turbulence dissipation
κ = thermal conductivity
λ = Taylor microscale
μ = viscosity
ρ = density
τ = shear stress
ϕ = random number with uniform distribution
ω = vorticity

Subscripts

d = dilatational
f = reference
s = solenoidal
t = derivative with respect to t
X, Y, Z = derivative with respect to X, Y, and Z
x, y, z = derivative with respect to x, y, and z

Superscripts

a = advective flux
v = viscous flux
$\breve{}$ = mapped space variable
$\tilde{}$ = Favre-averaged property
$\bar{}$ = Reynolds-averaged property
$'$ = Reynolds fluctuating property
$''$ = Favre fluctuating property
$+$ = normalized with wall coordinate

Introduction

IN the past two decades, direct numerical simulation (DNS) has become a viable research tool for the study of low- and moderate-Reynolds-number turbulent flows that has helped increase the physical understanding of various flows and has supplied a large database for model development and validation. (See, for example, Moin and Mahesh[1] for a review.)

The viability of DNS is dependent on the existence of highly accurate methods. At first sight, DNS appears to be simple because the Navier–Stokes (N–S) equations are discretized directly without the use of turbulence models. However, turbulence is characterized by a large range of scales for which computation with a standard low-order scheme, which typically has large dispersion and dissipation

---

Presented as Paper 2004-0659 at the AIAA 42nd Aerospace Sciences Meeting, Reno, NV, 5–8 January 2004; received 7 July 2004; revision received 24 November 2004; accepted for publication 4 January 2005.

[*] Visiting Assistant Professor, Division of Applied Mathematics; gjacobs2@dam.brown.edu. Member AIAA.

[†] Professor, Department of Mathematics.

[‡] Professor, Department of Mechanical and Industrial Engineering. Associate Fellow AIAA.

errors at short wavelengths, requires an unrealistically large number of grid points.[2]

High-order methods resolve small scales more efficiently than low order methods.[3] The rule of thumb is that Fourier and Chebyshev spectral methods require, asymptotically, two or π modes per wavelength, respectively, to resolve a sinusoid.[4] The question of how this changes with multidomain approximations was addressed in Refs. 5 and 6, where the optimal subdomain decomposition and order was sought to achieve a prescribed accuracy efficiently. The conclusion was that it is more efficient to use a higher order with larger subdomains and that the number of points per wavelength needed was not a rapidly varying function of the error desired. Depending on the work function chosen, the optimal number of points per wavelength is between about four and seven. These papers considered the interpolation error. More recently, Ainsworth[7] studied the dispersion errors of high-order discontinuous Galerkin approximations, concluding that exponential convergence of the phase error is obtained when the approximation order satisfies $2p + 1 \approx \kappa h k$, where h is the element size, k is the wave number, and $\kappa \approx 1$. This implies the rule of thumb of π modes per wavelength for the phase error as well. Numerical experiments on aeroacoustic wave propagation using spectral multidomain approximations in two space dimensions, for example, the experiments in Refs. 8 and 9, indicate that four to five points per wavelength are sufficient for accurate solutions. It is not known, however, what the similar rules of thumb are for the resolution of turbulent scales in the computation of compressible turbulence.

In this paper, we validate a Chebyshev multidomain spectral method (CMSM)[10–12] for the DNS of compressible turbulent flows. The method is spectrally accurate, has low dispersion, and can deal with complex geometries. Although methods of this type, namely, spectral/*hp* methods,[13,14] have been frequently used for DNS of incompressible transient/turbulent flows, the DNS of compressible turbulent flows has received little attention.

We will focus on a compressible isotropic turbulence and a compressible channel flow, two flows for which experimental and/or theoretical results are available. We will assess resolution requirements and discuss initialization issues for both flows. This information should serve as a benchmark for other general compressible spectral element codes[15,16] and as an indication of the resolution requirements for more complex simulations.

In the remainder of this paper, we first present the governing equations and discuss the numerical methodology. Then, the initialization of the isotropic turbulence for the CMSM is presented, followed by a comparison of results between the CMSM simulations and Fourier spectral simulations as presented by Blaisdell et al.[17] The channel flow initialization is discussed next, with a comparison of the results between the CMSM simulations and simulations by Moser et al.[18] with a spectral method. Finally, some concluding remarks are provided.

Governing Equations

We consider a compressible and Newtonian fluid with zero bulk viscosity that obeys the perfect gas equation of state. The N–S equations in dimensionless, conservation form for the fluid are

$$\boldsymbol{Q}_t + \boldsymbol{F}^a_x + \boldsymbol{G}^a_y + \boldsymbol{H}^a_z = (1/Re_f)\left(\boldsymbol{F}^v_x + \boldsymbol{G}^v_y + \boldsymbol{H}^v_z\right) \tag{1}$$

The equations for $\boldsymbol{Q} = [\rho, \rho u, \rho v, \rho w, \rho e]$ represent conservation of mass, momentum (in three directions), and total energy, respectively. The vectors $\boldsymbol{F}$, $\boldsymbol{G}$, and $\boldsymbol{H}$ represent the advective (superscript a) and viscous (superscript v) fluxes in three directions, and $\rho e = p/(\gamma - 1) + \rho(u^2 + v^2 + w^2)/2$ is the sum of the internal and kinetic energies. The equation of state is $p = \rho T/\gamma M_f^2$. All of the variables are normalized by reference length L_f, density ρ_f, velocity U_f, and temperature T_f scales. The reference Reynolds, Mach, and Prandtl numbers are defined by $Re_f = \rho_f U_f L_f/\mu$, $M_f = U_f/(\gamma R T_f)^{1/2}$, and $Pr = C_p \mu/\kappa$, respectively. In this formulation, we assume constant viscosity and specific heats.

Numerical Methodology

The computational methodology is described in detail in Refs. 10 and 19; this section provides a summary. The approximation begins with the subdivision of the region under consideration into nonoverlapping quadrilateral subdomains, or elements. Each element is then mapped onto a unit square by an isoparametric transformation using a linear blending formula. Under the mappings, Eq. (1) becomes

$$\breve{Q}_t + \breve{F}_X + \breve{G}_Y + \breve{H}_Y = 0 \tag{2}$$

where

$$\breve{Q} = J\boldsymbol{Q}, \qquad \breve{F} = X_x\boldsymbol{F} + X_y\boldsymbol{G} + X_z\boldsymbol{H}$$
$$\breve{G} = Y_x\boldsymbol{F} + Y_y\boldsymbol{G} + Y_z\boldsymbol{H}, \qquad \breve{H} = Z_x\boldsymbol{F} + Z_y\boldsymbol{G} + Z_z\boldsymbol{H} \tag{3}$$

Within an element, the solution values $\breve{Q}$ and the fluxes $\breve{F}$, $\breve{G}$, and $\breve{H}$ in Eq. (2) are approximated on separate grids. These grids are tensor products of the Lobatto grid, X_j, and the Gauss grid, $X_{j+1/2}$, mapped onto [0, 1]

$$\begin{aligned} X_j &= \tfrac{1}{2}\{1 - \cos[(j/N)\pi]\}, && j = 0, 1, \ldots, N \\ X_{j+\frac{1}{2}} &= \tfrac{1}{2}(1 - \cos\{[(2j+1)/N]\pi\}), && j = 0, 1, \ldots, N-1 \end{aligned} \tag{4}$$

On these grids, the Lagrange interpolating polynomials $l_j(\xi) \in \boldsymbol{P}_N$ and $h_{j+1/2}(\xi) \in \boldsymbol{P}_{N-1}$ are defined. Together with the choice of collocation points in Eq. (4), these polynomials represent a Chebyshev spectral approximation on each grid. The motivation for the staggered grid is that polynomial approximations of degree N that are to be differentiated once are represented on a Lobatto grid. Other quantities are of degree $N - 1$ and are represented on a Gauss grid. Thus, solution unknowns are collocated at Gauss points, whereas fluxes are collocated at Lobatto points. The solution is approximated by

$$\breve{Q}(X, Y, Z) = \sum_{i=0}^{N-1}\sum_{j=0}^{N-1}\sum_{k=0}^{N-1} \breve{Q}_{i+\frac{1}{2}, j+\frac{1}{2}, k+\frac{1}{2}} h_{i+\frac{1}{2}}(X) \times h_{j+\frac{1}{2}}(Y) h_{k+\frac{1}{2}}(Z) \tag{5}$$

From this polynomial, the solution values are computed at the Lobatto points. Although the solutions at the Lobatto points still describe a polynomial in $\boldsymbol{P}_{N-1}$, application of boundary and interface conditions add the extra degree of freedom to increase the polynomial order.

The inviscid fluxes are determined by evaluating the interpolant from Eq. (5) at the desired Gauss and Lobatto points. At points interior to the element, the fluxes are computed directly. Along element faces, Roe's approximate Riemann solver (see Ref. 20) is used to compute the flux using two solutions from the current and neighboring elements. For a detailed description of the role of the Riemann solver, we refer to Kopriva and Kolias.[19]

The computation of the viscous flux uses a two-step procedure. Because the reconstruction of the solution from the Gauss points onto the Lobatto points gives a discontinuous solution at the element faces, it is necessary to first construct a continuous piecewise polynomial approximation before differentiating. To construct the continuous approximation, the average of the solutions on either side of the interface is used as the interface value. The continuous solution is then differentiated to derive the derivative quantities needed for the viscous fluxes. Because differentiation reduces the polynomial order by one, it is natural to evaluate the differentiated quantities on the Gauss grid. Once the derivative quantities are evaluated at the Gauss points, a polynomial interpolant of form (5) is defined, so that the gradients can be evaluated at the Lobatto points. From the cell face values, the viscous fluxes are computed and combined with the inviscid fluxes to obtain the total flux.

Note that evaluating the gradients at the cell centers has two desired effects. First, it makes the evaluation of the divergence consistent with that used in the continuity equation. Second, the evaluation of the viscous fluxes will not require the use of subdomain corner points.

Boundary Conditions

Because the only wall boundary used in this paper is an isothermal no-slip wall, we will restrict our discussion to this boundary condition treatment. At solid wall boundaries, no-slip conditions are imposed for the velocity and an isothermal condition is imposed for the temperature. As before, the computations of the viscous and inviscid fluxes are treated separately.

The no-slip condition is enforced on the inviscid flux by imposing a flow on the other side of the wall with equal but opposite velocity. Because the wall is isothermal, the internal energy is set using the wall boundary temperature. Thus, if the evaluation of Eq. (5) at a vertical wall point $(X_0, Y_{j+1/2})$ gives $\boldsymbol{Q}_{0,j+1/2} = [\rho, \rho u, \rho v, \rho e]^T_{0,j+1/2}$, the external state $\boldsymbol{Q}_e = [\rho, -\rho u, -\rho v, \rho e]^T$ is defined, where $\rho e_{0,j+1/2}$ is given by $\rho T_{\mathrm{wall}}/[\gamma(\gamma-1)M_f^2] + [(\rho u)^2 + (\rho v)^2]/2\rho$. The advective flux is then determined with an Osher solver [Jacobs, G. B., Kopriva, D. A., and Mashayek, F., "A Conservative Isothermal Wall Boundary Condition for the Compressible Navier–Stokes Equations" (to be submitted)].

The viscous flux at a wall is computed in two stages, as described earlier. After the solution is reconstructed at the cell faces, the Dirichlet conditions $\rho u_{0,j+1/2} = \rho v_{0,j+1/2} = 0$ are set. Because the wall is isothermal, $T_{0,j+1/2} = T_{\mathrm{wall}}$ is then set. After the quantities ∇u, ∇v, and ∇T are interpolated back onto the faces, the viscous flux is added to the advective flux to obtain the total flux.

Isotropic Turbulence

In this section, we repeat a simulation of isotropic decaying turbulence that was performed in Ref. 17 with a Fourier pseudospectral method. Clearly, there is no need to use a multidomain code; however, the simulation will provide two valuable pieces of information. First, it provides a code validation for the simulation of compressible turbulence with the CMSM. Second, an indication of resolution requirements for DNS of turbulent flow with the CMSM (and, more generally, spectral/*hp* methods) is obtained through comparison with the results of the well-established Fourier spectral method. This indication can be used for simulations of turbulent flows in more complex geometries.

Initial Conditions

The simulation of isotropic turbulence is performed in a cube with periodic boundary conditions, which eliminates issues of specifying boundary conditions. The absence of specified boundary conditions, however, introduces the problem of generating the turbulence because no turbulent fluctuations can be specified at an inflow boundary. In addition, the simulation of decaying turbulence by definition lacks the presence of a source term that could generate turbulence.

Rogallo[21] and Blaisdell et al.[17] (BMR) found a solution to this problem by specifying initial conditions that produce a correlated flowfield with turbulent characteristics from specified initial energy spectra. For brevity, the details of this procedure are not repeated here. Rather, the equations involved and the case referred to as iga96 by BMR is presented here.

Initial conditions were produced by specifying initial solenoidal velocity E_s and dilatational velocity E_d, density E_ρ, and temperature E_T spectra. All spectra are top hat and have a constant nonzero contribution to wave numbers between $k = 8$ and 16. The amplitudes in this range are constant, but differ for the various spectra. For case iga96 by BMR, the amplitudes for the various spectra are given in Table 1.

Table 1 Initial values of various spectra for case iga96 from isotropic decaying turbulence simulations from BMR

Spectrum	Initial value
$E_s(k)$	2.8125×10^{-4}
$E_d(k)$	3.1250×10^{-5}
$E_\rho(k)$	1.2500×10^{-3}
$E_T(k)$	1.2500×10^{-3}

The Fourier coefficients for the solenoidal velocity field can be determined from the spectra as

$$\begin{bmatrix} \hat{u}_s(k) \\ \hat{v}_s(k) \\ \hat{w}_s(k) \end{bmatrix} = \begin{bmatrix} \dfrac{\alpha^{\mathrm{ran}} k k_2 + \beta^{\mathrm{ran}} k_1 k_3}{k k_{12}} \\ \dfrac{\beta^{\mathrm{ran}} k_2 k_3 - \alpha^{\mathrm{ran}} k k_1}{k k_{12}} \\ \dfrac{-\beta^{\mathrm{ran}} k_{12}}{k} \end{bmatrix} \tag{6}$$

where $\alpha^{\mathrm{ran}} = \sqrt{}[E_s(k)/4\pi k^2]e^{\boldsymbol{i}\phi_1}\cos(\phi_3)$ and $\beta^{\mathrm{ran}} = \sqrt{}[E_s(k)/4\pi k^2]e^{\boldsymbol{i}\phi_2}\sin(\phi_3)$. Here, $\phi_{1,2,3}$ are uniformly distributed numbers, $\boldsymbol{i}$ is the imaginary number $\sqrt{-1}$, k is the magnitude of the wave number vector (k_1, k_2, k_3), and k_{12} is expressed as $\sqrt{}(k_1^2 + k_2^2)$. If $k_{12} = 0$ then $\hat{u} = \alpha^{\mathrm{ran}}$ and $\hat{v} = \beta^{\mathrm{ran}}$. The Fourier coefficients for the dilatational velocity are given by

$$\begin{bmatrix} \hat{u}_d(k) \\ \hat{v}_d(k) \\ \hat{w}_d(k) \end{bmatrix} = \begin{bmatrix} \gamma^{\mathrm{ran}} k_1/k \\ \gamma^{\mathrm{ran}} k_2/k \\ \gamma^{\mathrm{ran}} k_3/k \end{bmatrix} \tag{7}$$

where $\gamma^{\mathrm{ran}} = \sqrt{}[E_d(k)/4\pi k^2]e^{\boldsymbol{i}\phi_4}$ and ϕ_4 is a uniformly distributed random number. The density and temperature Fourier coefficients are determined with

$$\hat{\rho}(k) = \sqrt{\left[E_\rho(k)/4\pi k^2\right]}e^{\boldsymbol{i}\phi_5}, \qquad \hat{T}(k) = \sqrt{\left[E_T(k)/4\pi k^2\right]}e^{\boldsymbol{i}\phi_6} \tag{8}$$

where ϕ_5 and ϕ_6 are, again, uniformly distributed random numbers.

The initial data are defined on the equidistant grid with coordinates, $x_i = (l_i - 1)L_f/N$, where $l_i = 1, \ldots, N$, and wave numbers, $k_i = 2\pi n_i/L_f$, where $n_i = -N/2 + 1, \ldots, N/2$, in each direction for $i = 1, 2, 3$. When the reference length $L_f = 2\pi$ is chosen, a three-dimensional discrete Fourier transform can be assembled from the coefficients in Eqs. (6–8) to determine the flowfield for u, v, w, ρ, and T at the equidistant Fourier grid. The resulting flowfield is correlated according to the top-hat spectrum.

The CMSM employs a Chebyshev grid. The initial flowfield at these points is obtained by performing an eighth-order Lagrangian interpolation on the Fourier grid. To verify whether this interpolation provided sufficient accuracy, the initial flowfield was interpolated back to the Fourier grid using spectral interpolation within each element. The energy spectra were determined by applying a Fourier transform on the interpolated values. These spectra were compared to the spectra obtained with the original Fourier expansion.

Figure 1 shows a comparison of the spectra for a $N = 64$ Fourier expansion and a CMSM grid with six equiextent subdomains in each direction and shows approximation orders of $\wp = 9$ and 13 on a linear scale (Fig. 1a) and a log scale (Fig. 1b). From Fig. 1a, it follows that interpolation leads to a 2% underestimation of the amplitude between $k = 8$ and 16 compared to the original Fourier expansion for both approximation orders in the CMSM. Both polynomial approximation orders show the same accuracy, which indicates that the difference with the original Fourier expansion is in a large part caused by the eighth-order interpolation to the nonuniform grid.

In the range for $k < 8$ and $k > 16$, the log scale shows that $\wp = 13$ is two orders of magnitude closer to the expected value of zero than $\wp = 9$. With spectral accuracy, one should expect four orders of magnitude closer to zero, but it is expected that the error is limited by the eight-order interpolation from the Fourier grid to the Chebyshev grid. The Fourier expansion clearly has better performance than $\wp = 13$ by approximating the spectrum nine orders of magnitude closer to zero. We are, however, not concerned with this difference, because in comparison to the amplitude of the spectrum of 3.125×10^{-4}, the values outside the interval are negligible in all cases.

Simulations

Simulations are performed on a domain with length 2π and with periodic boundary conditions in each direction. The computational

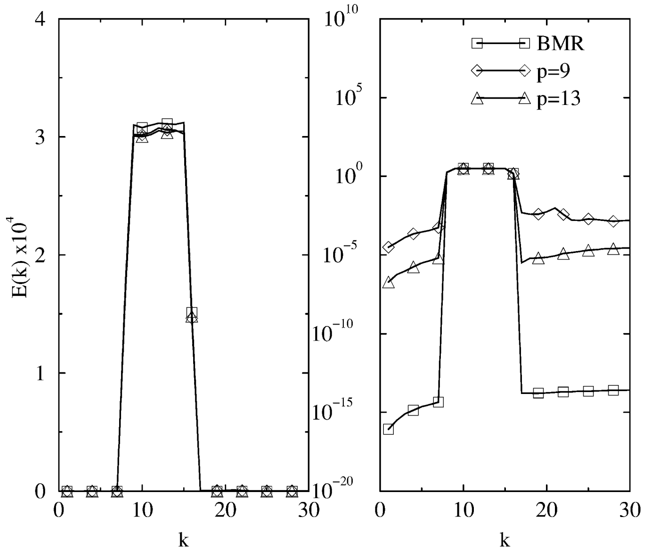

a) b)

Fig. 1 Comparison of initial energy spectrum in isotropic turbulence between BMR and CMSM with $\wp = 9$ and 13 on an a) linear and b) log scale.

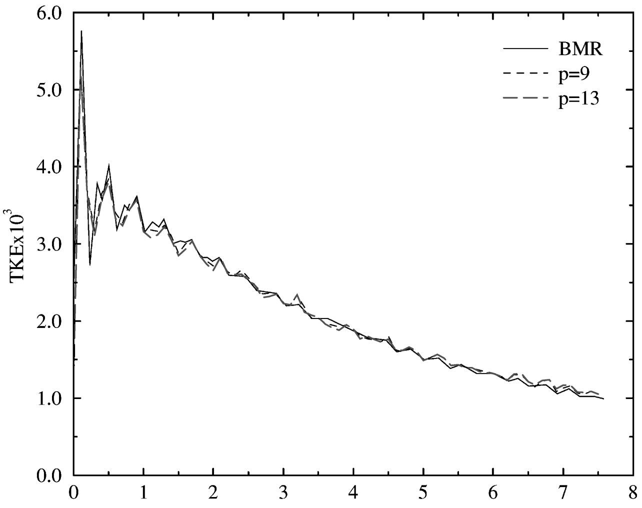

Fig. 2 Comparison of TKE in isotropic turbulence between BMR and CMSM with $\wp = 9$ and 13.

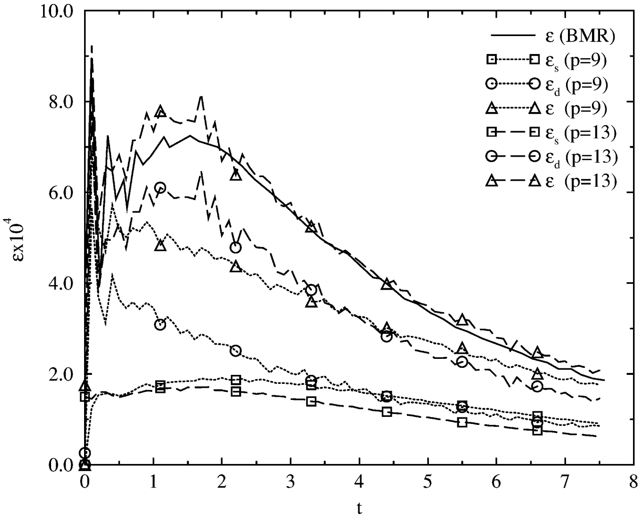

Fig. 3 Comparison of turbulence dissipation rate ϵ in isotropic turbulence between BMR and CMSM with $\wp = 9$ and 13; for CMSM, contributions of both solenoidal, ϵ_s, and dilatational, ϵ_d, dissipation rates.

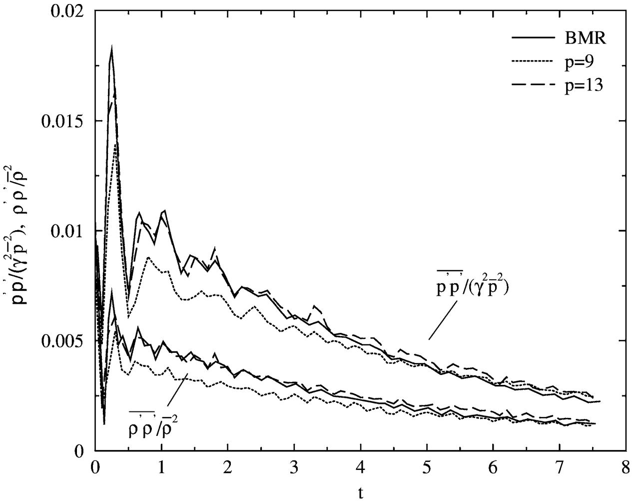

Fig. 4 Comparison of pressure variance, $\overline{p'p'}/(\gamma^2\bar{p}^2)$, and density variance, $\overline{\rho'\rho'}/(\bar{\rho}^2)$, in isotropic turbulence between BMR and CMSM with $\wp = 9$ and 13.

domain is divided into six equiextent subdomains in each direction. Two polynomial orders, $\wp = 9$ and 13, have been tested. The initial conditions are set as described earlier. The average initial temperature is $\bar{T}_0 = 1.0$, which leads to an initial fluctuation Mach number, $Ma_0 = 0.05$. Ma_0 is defined as

$$Ma_0 = \sqrt{\overline{u_i''u_i''}}/c(\bar{T}_0) \tag{9}$$

which is written in index notation. The double prime indicates a fluctuating Favre variable, and $c(\bar{T})$ is the speed of sound based on the average temperature. The computational Reynolds number Re_f is set to 2357. The Reynolds number based on the Taylor microscale λ is initially $Re_\lambda \sim 20$.

The results, obtained by integrating from the initial flow state, are compared to those of BMR, who used a Fourier spectral method with $N = 96$. Figure 2 shows a comparison of the turbulence kinetic energy (TKE) $= 1/2\overline{u_i''u_i''}$, vs time for the three cases. It is observed that the TKEs are in good agreement for all three cases. The TKE shows the well-known exponential decay[22] in time, which is due to dissipation. The wavy pattern of the TKE is a result of the exchange between the kinetic energy and the internal acoustic energy, also known as pressure dilatation.[23] The good prediction of TKE even by the low-order CMSM is somewhat surprising, but, as mentioned in Ref. 1, TKE is generally predicted well, even by lower-order methods.

A better measure of the CMSM's performance is given by comparing the evolution of the dissipation rate ϵ with time. In compressible turbulence, the solenoidal ϵ_s and dilatational ϵ_d are the two major contributors to the total dissipation ϵ. Other higher-order contributions turn out to be zero for homogeneous turbulence. Thus, ϵ may be expressed as the sum of ϵ_s and ϵ_d,

$$\epsilon = \underbrace{\frac{1}{Re_f}\overline{\omega_i'\omega_i'}}_{\epsilon_s} + \underbrace{\frac{4}{3}\frac{1}{Re_f}\overline{\frac{\partial u_i''}{\partial x_i}\frac{\partial u_j''}{\partial x_j}}}_{\epsilon_d} \tag{10}$$

where ω_i' is the fluid vorticity fluctuation. Figure 3 shows that the results for $\wp = 9$ clearly underpredict ϵ over the entire simulation time as compared to the prediction by BMR. The results for $\wp = 13$, however, compare well. Inspection of the ϵ_s and ϵ_d contributions to ϵ shows that the main difference between the two CMSM cases is in the prediction of ϵ_d. The simulation with $\wp = 9$ is not able to capture high-frequency acoustic waves, which leads to an underestimation of ϵ_d. Increasing the approximation order to $\wp = 13$ leads to a significant increase of the dilatational dissipation, whereas ϵ_s decreases slightly. Because ϵ agrees well with the results by BMR, it is assumed that the flow is resolved well enough. Figure 4 confirms

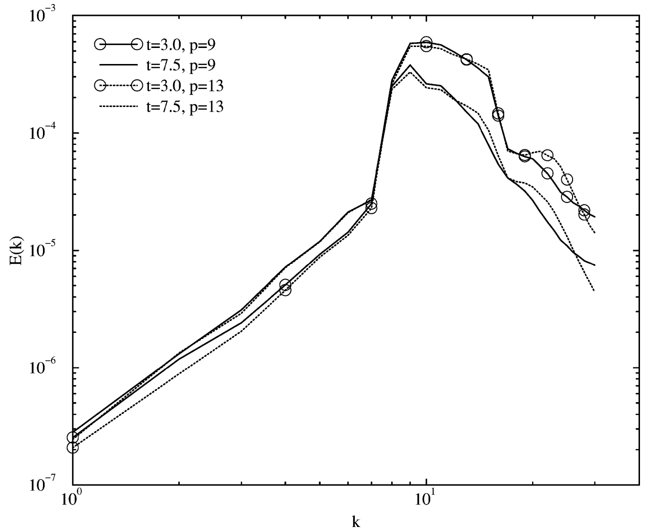

Fig. 5 Comparison of energy spectra $E(k)$ vs wave number k at $t = 3.0$ and 7.5 for CMSM with $\wp = 9$ and 13 in isotropic turbulence.

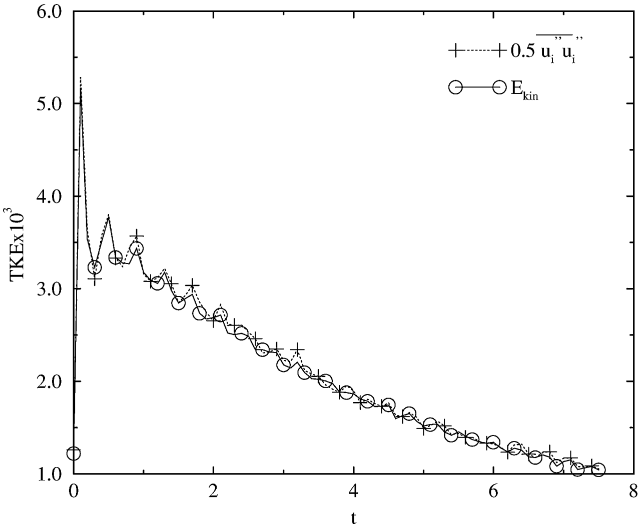

Fig. 6 Comparison of TKE in isotropic turbulence computed with $0.5\overline{u_i'' u_i''}$ and $E_{kin} = 0.5 \int_0^\infty E(k)\,dk$ for $\wp = 13$.

that $\wp = 9$ does not capture the acoustic waves well because both the pressure variance, $\overline{p'p'}/(\gamma^2\bar{p}^2)$, and the density variance, $\overline{\rho'\rho'}/(\bar{\rho}^2)$, are underestimated over the whole time interval. The case with $\wp = 13$ again performs far better, and approximates BMR's solution well.

Figure 5 shows the energy spectra for both CMSM cases at $t = 3.0$ and 7.5. At these times, the Reynolds numbers based on the Taylor microscale are 11.6 and 9.2, respectively. Unfortunately, no data for BMR's case are available for comparison. Figure 5 shows that the energy spectra are similar for wave numbers up to $k \sim 16$. Because TKE is one-half of the integrated area under the $E(k)$ curve, and because the magnitude of this integral is mainly determined by the contribution of $E(k)$ up to $k = 16$, the similarity of the spectra explains the similarity of the TKE trend for $\wp = 9$ and 13 in Fig. 2. At higher wave numbers, the case with $\wp = 13$ shows increased energy compared to $\wp = 9$. Because ϵ may alternatively be computed by integrating the area under the curve $k^2E(k)$, also known as the dissipation spectrum, and because $E(k)$ at high k contributes significantly to the integral due to the k^2 term, the increased amplitude in the energy spectrum for $k > 16$ explains the difference in ϵ. Computing ϵ from the dissipation spectrum offers a means to study resolution by inspecting the energy spectrum at large k. If the spectrum shows a sharp drop off at large k, this indicates that most dissipation is captured because the contribution of $E(k)$ in the dissipation spectrum will be small. Memory limitations restrict the computation of the spectrum to $k = 30$, but $E(k)$ clearly shows a sharp drop up to $k = 30$ for $\wp = 13$, whereas $\wp = 9$ flattens out at higher wave numbers.

An interesting feature of the spectrum is that, unlike what one would expect, the spectrum does not fill out at low wave numbers. This was explained by BMR through the association of vorticity with the solenoidal velocity field and the acoustic mode with the dilatational velocity field: Vorticity has both a mechanism for generating large scales through vortex stretching and smaller length scales through vortex merging. The solenoidal spectrum, thus, fills out at both low and high wave numbers. The acoustic mode, however, has only a mechanism for filling out the high wave number dilatation spectrum through nonlinear steepening of acoustic waves. In this particular computation, it is clear from the dissipation spectrum that dilatation dominates and determines the spectrum at $k > 16$ for a large part, thus explaining the relatively small filling of the spectrum at low wave numbers.

To verify the spectrum, TKE is computed with $E(k)$ as explained earlier and compared with the direct computation of TKE for $\wp = 13$. Figure 6 shows that the TKE computed from the spectrum is slightly smaller than the TKE computed directly. The difference, however, is small and is attributed to the cutoff of $E(k)$ at $k = 30$. The good comparison of the TKEs indicates a correct energy spectrum trend.

In conclusion, $\wp = 13$ resolves the flow significantly better than $\wp = 9$. Note that $\wp = 13$ compares well with the results by BMR, who used a Fourier spectral method with $N = 96$. The good dropoff in the energy spectrum at $k = 30$ suggests that at $\wp = 13$, 90 Lobatto points (6 subdomains times 15 Lobatto points) resolve the flow, that is, $90/30 = 3$ points per wavelength. This result is consistent with the asymptotic result for the Chebyshev spectral approximation, as described in the Introduction.

Channel Flow

This section presents results on the compressible flow between parallel plates, also known as channel flow. For incompressible flow, the N–S simulations (without models) have been quite extensive. Some of the key works include that of Kim et al.,[24] who performed DNS of the fully turbulent flow at $Re_f = 3300$. They found excellent comparison of the mean flow and first-order moments with experimental data and theoretical models, such as the universal law of the wall. Jimenez and Moin[25] investigated the minimal computational domain necessary to sustain turbulence in the channel flow. They observed longitudinal vortex structures, which they related to the so-called high-speed streaks near the wall. Moser et al.[18] performed studies at higher Reynolds numbers including simulations at the Reynolds numbers based on the skin-friction velocity of $Re_\tau = 200$, 500, and 700. In Ref. 13, a resolution study with a spectral element method was employed on the configuration in Ref. 25.

The DNS of compressible channel flow was initiated by Huang et al.[26] They performed DNS on the supersonic channel flow at two different Reynolds numbers and found that compressibility effects are limited to inertial effects, which are small. Recently, some studies have appeared in literature for subsonic flow, which were mainly used for code or model verification, for example, those of Gamet et al.[27] and Lenormand et al.[28]

In this section, the subsonic compressible channel flow is simulated at a Reynolds number of $Re_f = 3000$ based on the channel half-width L_f and the average velocity in the channel u_b. The Mach number Ma_f is chosen to be 0.4, and it is based on the bulk velocity u_b and the wall temperature T_{wall}. The purpose of the simulation is to validate and to assess resolution requirements for simulations with the CMSM in an inhomogeneous turbulent flow.

Computational Model

Our simulations follow the computational model outlined in Ref. 13 for the DNS of the incompressible channel flow with a spectral element method. The geometry is represented by a rectangle with nondimensional lengths $L_x = 2$, $L_y = 2$, and $L_z = 4$ in the wall normal, spanwise, and streamwise directions, respectively.

In Ref. 13, a grid of 12 elements in the wall normal direction, 10 elements in the spanwise periodic direction, and an $N = 64$ Fourier expansion in the streamwise periodic direction was employed. The element distribution in the wall normal direction was of a cosine form to account for the higher flow gradients near the wall. In the periodic directions, a uniform grid was employed.

In the simulation presented here, the same element distribution as in Ref. 13 is employed. However, the CMSM is used for the approximation in the streamwise direction as opposed to the Fourier spectral method. Based on the simulations in the preceding section of the isotropic turbulence, a 10 subdomain grid decomposition was chosen for simulation with the CMSM to obtain a resolution similar to the Fourier grid resolution in Ref. 13. To achieve a resolved flow, it was shown in Ref. 13 that a polynomial approximation of $\wp = 10$ is sufficient. This section presents results for $\wp = 6$ and 10.

Enforcing periodicity in the streamwise direction is not trivial because a negative pressure gradient sustains the channel flow, which creates a nonperiodic inhomogeneity. It can be shown by integration of the N–S equations over the width of the channel that specifying a constant source term leads to a mass flux that is time dependent.[28] This makes the analysis of the flow at a constant Reynolds number impossible. For the mass flux to be time independent, it was shown that the forcing term has to be time dependent. The algorithm presented in Ref. 28 for maintaining a constant mass force is employed here as well. The wall boundary condition is isothermal.

Initiation and Transition to Turbulence

The velocity field is initialized with the laminar parabolic Poiseuille profile with a random disturbance in the streamwise velocity as

$$u(y) = -6[(y/2)^2 - y/2](1 + \epsilon) \tag{11}$$

where ϵ is a 10% random disturbance. The random disturbance is introduced to accelerate the transition to a turbulent flow. For the temperature, the laminar Poiseuille profile is initially specified as

$$T(y) = T_{\text{wall}} + \{[3(\gamma - 1)/4Pr][1 - (y - 1)^4]\} \tag{12}$$

where $T_{\text{wall}} = 6.25$ is the wall temperature and $Pr = 0.72$ is the Prandtl number. The density is initially set constant. The pressure follows from the constant density, the initial temperature, and the ideal gas law.

With this initial flowfield and the resolution described in the preceding section, the initial disturbance damps out at the intended Reynolds number of $Re_f = 3000$, and the flow returns to its laminar state. Increasing the Reynolds number to $Re_f = 6000$ to force transition does not lead to transition within computational times that are feasible. This is not unexpected because the critical Reynolds number for incompressible transition is $Re_f = 5772$ (Ref. 29) and compressibility tends to increase this critical Reynolds number.

Rather than increasing the Reynolds number even more, the flow is simulated at a lower resolution of $\wp = 2$ in the hope that truncation error of the scheme with act as a sufficiently large disturbance required for transition. From Fig. 7, which shows the average skin-friction coefficient c_f plotted vs time, it is observed that this approach works: Up to time $t \sim 20$, the flow maintains its laminar skin-friction coefficient of $c_f = 3/Re_f = 0.001$, but for times $t > 20$, c_f increases, indicating transition. At time $t \simeq 80$, c_f levels off at the expected turbulent c_f of approximately 0.042. Interpolation of the solution at $\wp = 2$ to that at $\wp = 10$ determines a turbulent initial condition for the simulation at $\wp = 10$. The $\wp = 2$ solution is interpolated gradually to $\wp = 10$ in increments of two accompanied by a short simulation. Results of the quasi-steady-state channel flow obtained by simulating from this initial condition are presented in the next section.

Simulations

The results of the simulations are presented for $\wp = 6$ and 10 and are compared to the results of Moser et al.[18] (MKM).

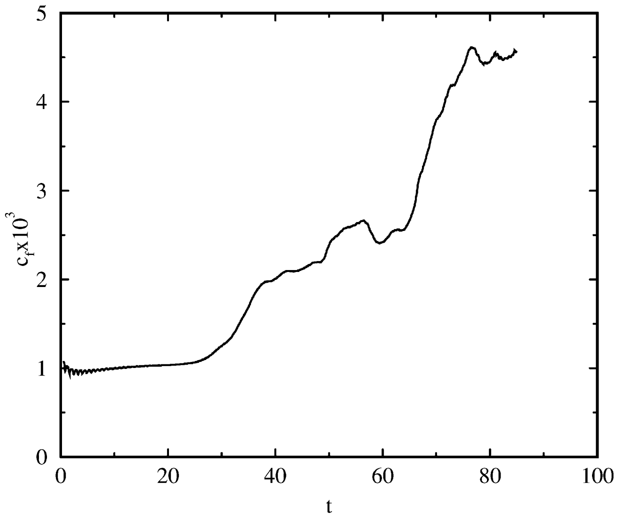

Fig. 7 Temporal variation of skin-friction coefficient c_f with transition to turbulence in channel flow.

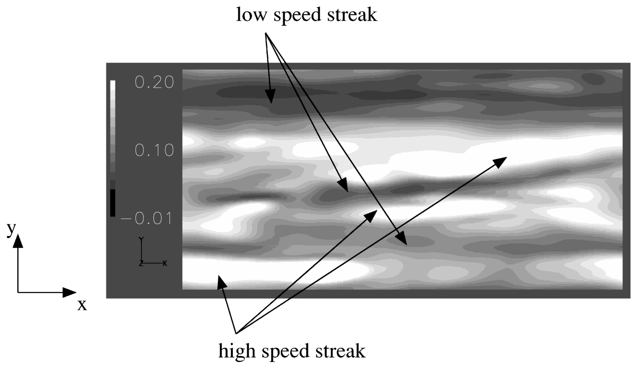

Fig. 8 Instantaneous streamwise u-velocity contour at $z = 0.01$ in channel flow for $\wp = 10$.

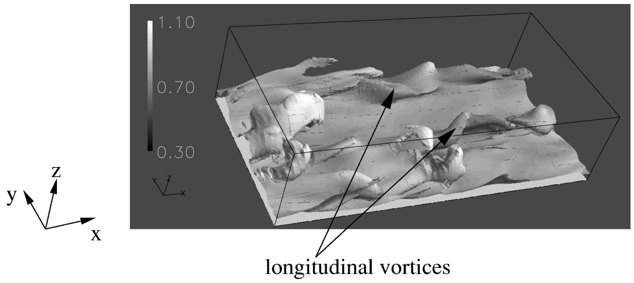

Fig. 9 Instantaneous temperature isocontours in channel flow colored with streamwise u-velocity component for $\wp = 10$.

Instantaneous Flowfield

Figure 8 shows the u-velocity contours close to the wall at $z = 0.01$ for $\wp = 10$. Clearly visible is the streaky pattern observed in other works, for example, Refs. 22, 24, and 25, that is caused by the long vorticial structures. Three high-speed and low-speed streaks may be observed. An approximate separation of the streaks is 0.33 in y direction, which is computed as the ratio of the two length units width of the computational domain over the six streaks. This separation is in good agreement with Ref. 24, where the separation was reported to be 0.3. In Fig. 9, the longitudinal vortices are shown by temperature isocontours colored with the u velocity for $\wp = 10$. The distance between these two long vortices is approximately 0.5 in the y direction, again showing a good agreement with the reported value of 0.5 in Ref. 24.

Comparison of Average Flowfield

The Favre-averaged velocity scaled with the skin-friction velocity u^+ plotted vs the wall normal coordinate z is shown in Fig. 10a for

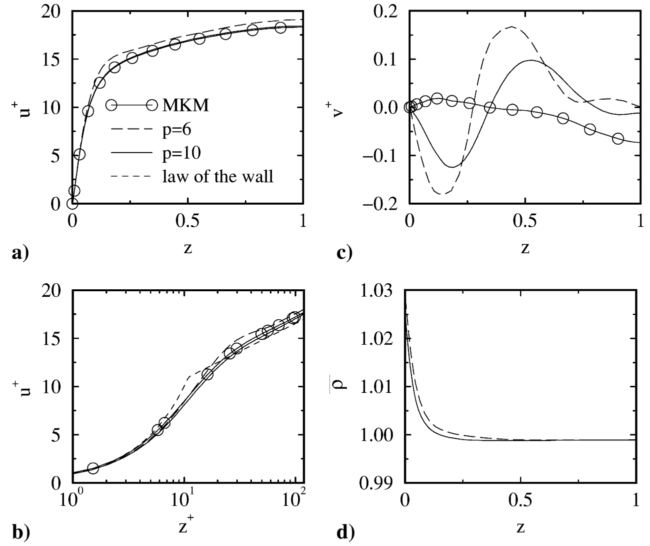

Fig. 10 Various averaged flow variables in channel flow in wall normal direction: u^+ vs a) z and b) z^+, c) v^+ vs z, and d) $\bar{\rho}$ vs z.

$\wp = 6$ and 10. Here, the skin-friction velocity u_τ is defined as

$$u_\tau = \sqrt{\tau_{\text{wall}}/\rho_{\text{wall}}} \tag{13}$$

where τ_{wall} and ρ_{wall} are the average shear stress and density at the wall, respectively. It is observed that increasing the polynomial order leads to a closer agreement with MKM's results.

At $\wp = 6$, the skin-friction velocity u_τ is underpredicted. Furthermore, the solution is slightly asymmetric due to the upwinding properties (needed for stability of all compressible solvers) of the Roe solver. At $\wp = 10$, the solution shows increased symmetry, and the skin-friction velocity u_τ is accurately predicted as 0.062, within 3% of Dean's correlation[30] of 0.064. In Fig. 10b, the same velocity u^+ is plotted vs the wall coordinate z^+, defined as

$$z^+ = \rho_{\text{wall}} z u_\tau Re_f \tag{14}$$

It is observed that $\wp = 6$ slightly overpredicts the average velocity, but $\wp = 10$ is in excellent agreement with MKM's results and the theoretical law of the wall[22] given by

$$\begin{aligned} u^+ &= z^+, & z^+ &< 10 \\ u^+ &= 2.5\,\ell n\, z^+ + 5.5, & z^+ &> 10 \end{aligned} \tag{15}$$

Figure 10c compares the averaged spanwise v velocity scaled with u_τ, v^+, plotted vs the wall normal coordinate for $\wp = 6$ and 10 with MKM's result. At the symmetry line, the v^+ velocity by MKM is not zero, whereas symmetry considerations suggest a zero v^+ velocity. In the work of MKM, this discrepancy was claimed to be an indication of the accuracy of the computation. The error is on the order of 1% of the average u^+. The CMSM predicts a symmetric v^+ slightly closer to the zero symmetry value than MKM's result. The trend of v^+, however, shows differences with the result of MKM, which most likely result from the different approximations in the streamwise direction through the CMSM here vs the Fourier spectral method used by MKM. Increasing $\wp$ from 6 to 10 decreases the peak values of v^+ from 2 to 1% of the average u^+ velocity.

Figure 10d shows the averaged density $\bar{\rho}$ for both polynomial orders. Because MKM's simulations are incompressible, no comparison with their results is available. Observe that there is approximately a 2.3% increase in density near the wall for $Ma_f = 0.4$, indicating a relatively small effect of compressibility. Increasing $\wp$ from 6 to 10 leads to less than a 0.02% difference in the density distribution.

Comparison of Turbulence Statistics

Figure 11 shows that the Favre fluctuating rms velocity components, normalized with u_τ, compare well for $\wp = 10$ with the results presented by MKM. At $\wp = 6$, the main discrepancy is in the peak value of u''^+_{rms}. However, the trends for the various rms components are comparable. A similar conclusion may be drawn for the off-diagonal Reynolds stress component $\widetilde{u''w''}^+$ for $\wp = 6$ presented in Fig. 12, which shows an overprediction of its peak value close to the wall as compared to the results of MKM. It is observed that the overpredicted $\widetilde{u''w''}^+$ near the wall is compensated for farther away from the wall, where $\widetilde{u''w''}^+$ is underpredicted. This discrepancy seems to be related to the positive values of $\widetilde{u''v''}^+$, which should theoretically be zero. The positive $\widetilde{u''v''}^+$ is, in turn, most likely related to the aforementioned asymmetry in the $\tilde{u}$-velocity profile. At $\wp = 10$, the asymmetry is far less, but the $\widetilde{u''w''}^+$ Reynolds stress component is still larger than the result predicted by MKM. However, for $\wp = 10$, there is no compensation farther away from the wall as is observed for $\wp = 6$. Furthermore, $\widetilde{u''v''}^+$ is much closer to its theoretical zero value than that for $\wp = 6$. Results from incompressible DNS simulations in Ref. 24 and experimental measurements in Ref. 31 indicate that $\widetilde{u''v''}^+$ may be larger than that predicted by MKM: For example, in Ref. 31, a peak value of $\widetilde{u''v''}^+ = -0.78$ is predicted, which is comparable to the peak value of -0.79 predicted by the CMSM.

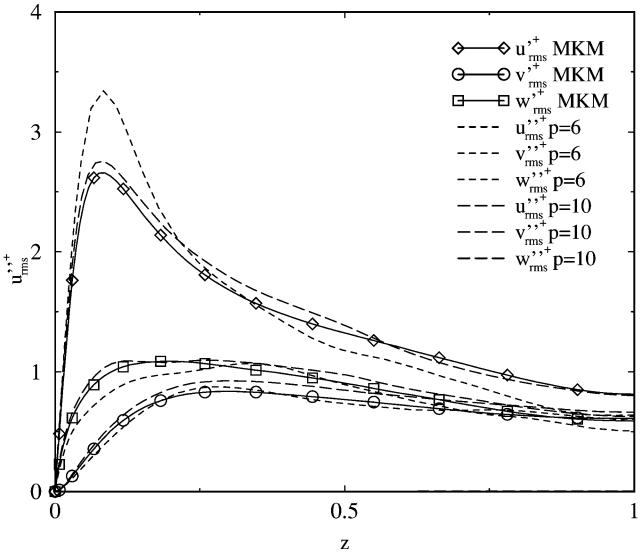

Fig. 11 Favre fluctuation rms velocities normalized with u_τ, u''^+_{rms}, v''^+_{rms}, and w''^+_{rms} for $\wp = 6$ and 10, compared with Reynolds fluctuating velocities normalized with u_τ, u'^+_{rms}, v'^+_{rms}, and w'^+_{rms} from MKM vs z in channel flow.

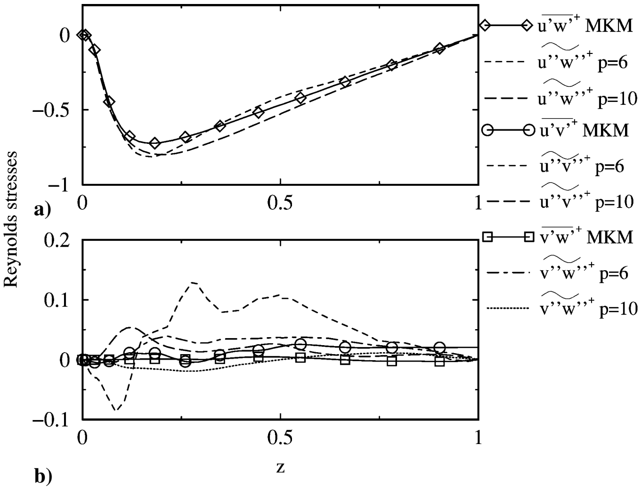

Fig. 12 Favre-averaged Reynolds stresses normalized with u_τ, a) $\widetilde{u''w''}^+$, b) $\widetilde{u''v''}^+$, and b) $\widetilde{v''w''}^+$ compared with the Reynolds averaged Reynolds stresses normalized with u_τ, a) $\overline{u'w'}^+$, b) $\overline{u'v'}^+$, and b) $\overline{v'w'}^+$ from MKM vs z in channel flow.

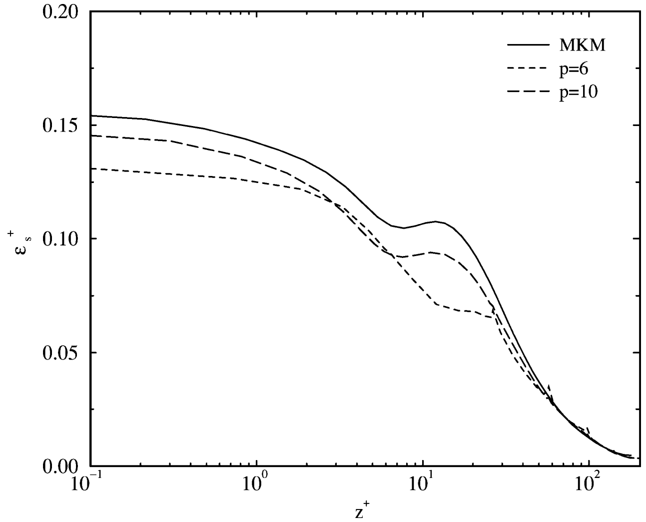

Fig. 13 Reynolds-averaged solenoidal dissipation rate, $\epsilon_s^+ = (1/Re_f)\,\overline{\omega_i'\omega_i'}^+$ for $\wp = 6$ and 10 compared with MKM vs z^+.

Both the studies by Gamet et al.[27] and by Lenormand et al.[28] predict higher peak values and show differences in the rms velocities with previous incompressible simulations as well. Thus, although one would expect DNS results to compare well with a deviation of, for example, less than 1%, various experimental and numerical studies show this not to be the case.

Finally, as a good measure of the resolution in Fig. 13, we plot the solenoidal part of the dissipation (10) normalized with u_τ. Note that the dilatational terms and terms that appear due to inhomogeneity in the dissipation rate do not exceed 1% of the peak value of the solenoidal dissipation, confirming the relatively small influence of dilatation on the compressible channel flow. As in the isotropic turbulence problem, the lower-order polynomial underpredicts dissipation, whereas the result for $\wp = 10$ underpredicts the dissipation less. Furthermore, at $\wp = 10$, the trends are the same and the skin friction is expected to be lower due to the increased density near the wall. The main difference between $\wp = 6$ and 10 is found near the wall where $\wp = 6$ is not able to capture the high-velocity gradient in the viscous sublayer as well as $\wp = 10$ does.

Assessment of Resolution

In conclusion, the results at $\wp = 10$ compare well to MKM's results and the expected channel behavior. MKM reported a good dropoff in the one-dimensional streamwise and spanwise spectra at wave numbers $k_x = 30$ and $k_y = 90$, respectively. The stream- and spanwise dimensions of the computational domain in our simulation are $L_x = 4$ and $L_y = 2$, that is, the number of waves at the dropoff wave numbers in our domain are $L_x k_x / 2\pi = 19$ and $L_y k_y / 2\pi = 28$. In both directions, 120 Lobatto points are used to resolve the flow. Thus, a resolution of six and four points per wavelength (ratio of the number of waves in the domain over the number of Lobatto points) sufficiently resolves the flow in the stream- and spanwise directions. Again, this is consistent with what one would expect for a multidomain Chebyshev spectral approximation, as discussed in the introduction.

Conclusions

To initiate the DNS study of three-dimensional compressible turbulent flows with multidomain spectral methods, simulations are first conducted on an isotropic decaying turbulence to validate the code and assess the resolution requirements. The initial conditions are determined on a Fourier grid in the wave space, and the physical flowfield is determined through a Fourier transform. The physical flowfield interpolated to the Chebyshev grid with an eighth-order Lagrangian interpolation scheme provides an accurate initial turbulence. The flow, computed with six subdomains and a polynomial order approximation $\wp = 13$ in each direction resolves the flow well when compared to a Fourier spectral method with $N = 96$.

For further validation of the code and assessment of resolution needed for the CMSM to compute inhomogeneous turbulence, a fully turbulent channel flow simulation is performed at Reynolds and Mach numbers of $Re_f = 3000$ and $Ma_f = 0.4$, respectively, based on the channel half-width, the bulk velocity, and the wall temperature. Transition to turbulence from the laminar initial state is obtained by simulating at low resolution so that the truncation errors of the scheme introduce the flow disturbances required for transition. By the interpolation of the result to a grid with a higher-order polynomial and continuation of the simulation, the resolved resolution result is obtained. If the high resolution is employed from the initial time, transition from the laminar initial state does not occur within feasible computational times for Reynolds numbers up to $Re_f = 6000$. Comparison of the turbulent statistics shows acceptable agreement with previously published results. Compressibility effects at this Mach number are limited to a 2% increase in the averaged density near the wall and a maximum 1% contribution of the nonsolenoidal dissipation terms to the total dissipation.

Based on the energy spectra in the periodic directions, the computations show that from 3 to 6 points per wave number are sufficient for an order of approximation that varies from 13 to 10, respectively. These resolution requirements can serve as an indicator for more complex geometries by recognizing flow parts that resemble a homogeneous turbulence and wall bounded turbulence and by using the appropriate points per wave number in those regions.

Acknowledgments

Support for this work was provided by the U.S. Office of Naval Research under Grant N00014-99-1-0808, with G. D. Roy as Technical Monitor; by the National Science Foundation under Grant CTS-0237951, with T. J. Mountziaris as Program Director; and by the Florida State University School for Computational Science and Information Technology by a grant of resources on the IBM pSeries 690 Power4-based supercomputer Eclipse. Finally, the authors extend appreciation to G. E. Karniadakis for fruitful discussions.

References

[1] Moin, P., and Mahesh, K., "Direct Numerical Simulation: A Tood in Turbulence Research," *Annual Review of Fluid Mechanics,* Vol. 30, 1998, pp. 539–578.

[2] Sarkar, S., and Hussaini, M. Y., "Computation of the Acoustic Radiation from Bounded Homogeneous Flows," *Computational Aeroacoustics*, edited by J. C. Hardin and M. Y. Hussaini, Springer-Verlag, Berlin, 1993, pp. 335–355.

[3] Hesthaven, J. S., "High-Order Accurate Methods in Time-Domail Computational Electromagnetics. A Review," *Advances in Imaging and Electron Physics*, Vol. 127, 2003, pp. 59–123.

[4] Gottlieb, D., and Orszag, S., *Numerical Analysis of Spectral Methods: Theory and Applications*, Society for Industrial and Applied Mathematics, Philadelphia, 1977, pp. 35–37.

[5] Wasberg, C.-E., and Gottlieb, D., "Optimal Decomposition of the Domail in Spectral Methods for Wave-Like Phenomena," *SIAM Journal on Scientific Computing*, Vol. 22, No. 2, 2000, pp. 617–632.

[6] Fischer, P., and Gottlieb, D., "On the Optimal Number of Subdomains for Hyperbolic Problems on Parallel Computers," *International Journal of Supercomputer Applications and High Performance Computing*, Vol. 11, No. 1, 1997, pp. 65–76.

[7] Ainsworth, M., "Dispersive and Dissipative Behavior of High Order Discontinuous Galerkin Finite Element Methods," *Journal of Computational Physics*, Vol. 198, No. 1, 2004, pp. 106–130.

[8] Bismuti, P., and Kopriva, D., "Solution of Acoustic Scattering Problems by a Staggered-Grid Spectral Domain Decomposition Method," *Second Computational Aeroacoustics (CAA) Workshop on Benchmark Problems*, edited by J. C. Hardin, R. Ristorcelli, and C. K. W. Tam, NASA CP 3352, 1997, pp. 69–78.

[9] Rasetarinera, P., Kopriva, D., and Hussaini, M., "Discountinuous Spectral Element Solution of Acoustic Radiation from Thin Airfoils," *AIAA Journal*, Vol. 39, No. 11, 2001, pp. 2070–2075.

[10] Kopriva, D. A., "A Staggered-Grid Multidomain Spectral Method for the Compressible Navier–Stokes Equations," *Journal of Computational Physics*, Vol. 143, No. 1, 1998, pp. 125–158.

[11] Jacobs, G. B., Kopriva, D. A., and Mashayek, F., "A Comparison of Outflow Boundary Conditions for the Multidomain Staggered-Grid Spectral Method," *Numerical Heat Transfer, Part B*, Vol. 44, No. 3, 2003, pp. 225–251.

[12] Jacobs, G. B., Kopriva, D. A., and Mashayek, F., "Compressible Subsonic Particle-Laden Flow over a Square Cylinder," *Journal of Propulsion and Power*, Vol. 20, No. 2, 2004, pp. 353–359.

[13] Karniadakis, G. E., and Sherwin, S. J., *Spectral/hp Element Methods for CFD,* Oxford Univ. Press, New York, 1999.

[14] Deville, M. O., Fischer, P. F., and Mund, E. H., *High-Order Methods for Incompressible Fluid Flow*, Cambridge Univ. Press, Cambridge, England, U.K., 2002.

[15] Bassi, F., and Rebay, S., "A High-Order Accurate Discontinuous Finite Element Method for the Numerical Simulation of the Compressible Navier–Stokes Equation.," *Journal of Computational Physics*, Vol. 131, No. 2, 1997, pp. 267–279.

[16] Hesthaven, J., and Warburton, T., "Nodal High-Order Methods on Unstructured Grids. I. Time-Domain Solution of Maxwell's Equations," *Journal of Computational Physics*, Vol. 181, No. 2, 2002, pp. 186–221.

[17] Blaisdell, G. A., Mansour, N. N., and Reynolds, W. C., "Numerical Simulation of Compressible Homogeneous Turbulence," Dept. of Mechanical Engineering, Rept. TF-50, Stanford Univ., Stanford, CA, 1991.

[18] Moser, R., Kim, J., and Mansour, N. N., "Direct Numerical Simulation of Turbulent Channel Flow Up to $\mathrm{Re}_\tau = 590$," *Physics of Fluids*, Vol. 11, No. 4, 1999, pp. 943–945.

[19] Kopriva, D. A., and Kolias, J. H., "A Conservative Staggered-Grid Chebyshev Multidomain Method for Compressible Flows," *Journal of Computational Physics*, Vol. 125, No. 1, 1996, pp. 244–261.

[20] Roe, P. L., "Approximate Riemann Solvers, Parameter Vectors, and Difference Schemes," *Journal of Computational Physics*, Vol. 43, No. 2, 1981, pp. 357–372.

[21] Rogallo, R. S., "Numerical Experiments in Homogeneous Turbulence," NASA TM 81315, 1981.

[22] Nieuwstadt, F. T. M., *Turbulentie, Inleiding, in de Theorie en Toepassing van Turbulente Stromingen*, Epsilon Uitgaven, Utrecht, The Netherlands, 1992.

[23] Kida, S., and Orszag, S., "Energy and Spectral Dynamics in Decaying Compressible Turbulence," *Journal of Scientific Computing*, Vol. 7, No. 1, 1992, pp. 1–34.

[24] Kim, J., Moin, P., and Moser, R. D., "Turbulent Statistics in Fully Developed Turbulent Channel Flow at Low Reynolds Number," *Journal of Fluid Mechanics*, Vol. 177, 1987, pp. 133–166.

[25] Jimenez, J., and Moin, P., "The Minimal Flow Unit in Near-Wall Turbulenece," *Journal of Fluid Mechanics*, Vol. 225, 1991, pp. 213–240.

[26] Huang, P. G., Colemn, G., and Bradshaw, P., "Compressible Turbulent Channel Flows: DNS Results and Modelling," *Journal of Fluid Mechanics*, Vol. 305, 1995, pp. 185–218.

[27] Gamet, L., Ducros, F., Nicoud, F., and Poinsot, T., "Compact Finite Difference Schemes on Non-Uniform Meshs. Application to Direct Numrical Simulations of Compressible Flows," *International Journal for Numerical Methods in Fluids*, Vol. 29, No. 2, 1999, pp. 159–191.

[28] Lenormand, E., Sagaut, P., and Ta Phuoc, L., "Large Eddy Simulation of Subsonic and Supersonic Channel Flow at Moderate Reynolds Number," *International Journal for Numerical Methods in Fluids*, Vol. 32, No. 4, 2000, pp. 369–406.

[29] Orszag, S. A., "Accurate Solution of the Orr–Sommerfield Stability Equation," *Journal of Fluid Mechanics*, Vol. 50, 1971, pp. 689–703.

[30] Dean, R., "Reynolds Number Dependence of Skin Friction and Other Bulk Flow Variables in Two-Dimensional Rectangular Duct Flow," *Journal of Fluids Engineering*, Vol. 100, No. 2, 1978, pp. 215–223.

[31] Niederschulte, M. A., Adrian, R. J., and Hanratty, T., "Measurements of Turbulent Flow in a Channel Flow at Low Reynolds Numbers," *Experiments in Fluids*, Vol. 9, No. 4, 1990, pp. 222–230.

H. Chelliah
Associate Editor